



Impacts of catalyst and process parameters on Ni-catalyzed methane dry reforming via interpretable machine learning

Keerthana Vellayappan^{a,1}, Yifei Yue^{a,1}, Kang Hui Lim^a, Keyu Cao^a, Ji Yang Tan^a,
Shuwen Cheng^{a,b}, Tianchang Wang^a, Terry Z.H. Gani^a, Iftekhar A. Karimi^{a,*}, Sibudjing Kawi^{a,*}

^a Department of Chemical and Biomolecular Engineering, National University of Singapore, Singapore 119260, Singapore

^b School of Metallurgy, Northeastern University, Shenyang 100819, PR China

ARTICLE INFO

Keywords:

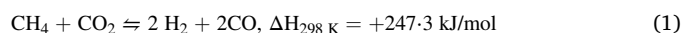
Machine Learning
Heterogeneous catalysis
Dry reforming of methane
Syngas
Catalyst design

ABSTRACT

Dry reforming of methane (DRM) is a promising technology for valorizing two potent greenhouse gases, namely CO₂ and CH₄. Although design principles for active and stable catalysts are well-established, predicting selectivity of DRM over competing side reactions that alter product H₂/CO ratio remains challenging. Here, we curate a set of 1638 data points from published literature and train tree regressor models to predict H₂/CO ratio as a function of 11 catalyst and process parameters. The CatBoost regressors achieved best prediction performance with R² = 0.91. Feature importance analysis reveals, in addition to well-known effects of process parameters on DRM performance, the potential roles of Ni particle size and loading in tuning H₂/CO ratio independently of reactant conversions. Our exploratory study highlights ability of data-driven ML models to unearth structure-property relationships in heterogeneous catalysis by isolating effects of individual design parameters in a manner that would be difficult to achieve experimentally.

1. Introduction

The adverse effects of global warming have prompted vigorous international efforts to counteract its harmful effects and foster sustainable development, such as the coordinated efforts to limit warming to 1.5 °C above pre-industrial temperatures [1]. Processes that can convert greenhouse gases such as CO₂ into useful chemical products have thus received intense interest in recent years as a possible means of decarbonizing the chemical industry [2]. For instance, the dry reforming of methane (DRM) (Eq. 1) is a promising alternative to steam methane reforming for the production of syngas (i.e., a mixture of CO and H₂) [3]. With a theoretical H₂/CO ratio of near unity, the syngas produced is well-suited for subsequent processing via oxo chemistry into acetic acid or aldehydes [4], or via Fischer-Tropsch chemistry into high-value liquid hydrocarbon products such as diesel and jet fuels [5,6].



In addition to noble metals such as Pt that are highly active catalysts for DRM, certain earth-abundant elements such as Ni also show reasonable activity but are prone to coking and sintering which cause

deleterious effects such as deactivation and reactor pressure buildup [7, 8]. Hence, strategies for improving the activity and stability of earth-abundant DRM catalysts by targeting their coking and sintering resistance have been broadly explored [4,5,9]. For instance, surface modification by redox-active oxides such as CeO₂ or ZrO₂ with high oxygen mobility can improve coke resistance by promoting the dissociation of CO₂ and subsequent gasification of deposited carbon by reactive oxygen species [10], and sintering can be physically inhibited by confinement within mesoporous channels [11]. Notably, both of these advantages can be simultaneously realized via encapsulation within a porous reducible oxide shell, in which the core-shell morphology plays a dual role of physically preventing sintering while also maximizing the fraction of Ni-reducible oxide interfacial sites that are active for CO formation [12–14].

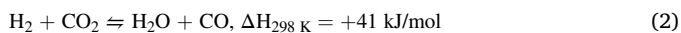
Another challenge associated with Ni-based DRM catalysts that has received much less attention is the tendency for the product syngas ratio (i.e., H₂/CO ratio) to fall below unity because of the parasitic reverse water-gas shift (RWGS) reaction (Eq. 2) that consumes H₂ and produces H₂O as an unwanted by-product [15]. A low syngas ratio is undesirable because the syngas stream must then be replenished with H₂ before it

* Corresponding authors.

E-mail addresses: cheiak@nus.edu.sg (I.A. Karimi), chekawis@nus.edu.sg (S. Kawi).

¹ These authors contributed equally.

can be used in downstream applications, leading to increased pre-treatment costs [16]. Within the open literature, there are relatively few papers that discuss the effects of catalyst properties on the syngas ratio and, more importantly, how they can be tuned to increase the syngas ratio [17,18]. While it is sometimes postulated that the syngas ratio is largely governed by the thermodynamics of the RWGS reaction rather than the nature of the catalyst itself [19,20], this is inconsistent with several reported observations of significantly different syngas ratios over different catalysts even at the same reaction conditions [21], which points to the possibility of targeted catalyst engineering to increase the selectivity of the DRM reaction over the RWGS reaction in a manner similar to how the thermodynamically favorable coking reaction can be inhibited over coking-resistant materials.



Machine learning (ML) has seen widespread use in materials design and discovery for its ability to uncover correlations across large datasets [22]. Within the field of heterogeneous catalysis, ML models have often been employed to overcome computational bottlenecks associated with density functional theory (DFT) calculations [23] by predicting computable physical properties [24] (e.g., adsorption energies) and reaction mechanisms [25] (i.e., based on estimated activation energies of possible elementary steps) from electronic or structural fingerprints. In a complementary approach, ML models can also be trained on experimental data, either extracted from published literature [26–28] or generated from high-throughput experimentation [29,30], to predict catalytic performance from process parameters and measurable catalyst properties [26,31]. This latter approach is particularly useful for multicomponent materials with complex architectures that cannot be accurately modeled by presently available computational methods (e.g., DFT). In all of these studies, model interpretability [31], as can be achieved by feature importance analyses of black-box ML model output, is crucial for developing qualitative scientific insights [28] that can in turn be leveraged by experimentalists to help develop improved catalysts and processes. Compared to inherently interpretable ML methods such as symbolic regression-based approaches [32–34], this two-step “gray-box” approach typically offers increased prediction accuracy across large and complex datasets [31].

In this work, we develop interpretable ML models to unearth structure-property relationships from the vast body of literature on Ni-catalyzed DRM. Specifically, we first gather from the open literature a comprehensive, high-quality dataset of catalyst properties, process parameters, and reactivity data, on which we then train tree regressor models (random forest – RF [35], gradient boosted regressor – GBR [36] and categorical tree regressor – CatBoost [37]) to predict reactant conversions and syngas ratios using catalyst properties and process parameters as features. We then apply *posteriori* model interpretation techniques [38] to illustrate how each feature influences syngas ratio and reactant conversions. In addition to reproducing the well-known effects of temperature, space velocity, and feed dilution on DRM performance, the partial dependence plots applied in our study also reveal Ni particle size as a potential handle for controlling syngas ratio independently of the effects of process operating conditions.

2. Method

2.1. Overall approach

We select three commonly used quantitative metrics of DRM catalyst performance, namely CH₄ conversion, CO₂ conversion, and syngas ratio (defined as the ratio of H₂ formation rate to CO formation rate), as our targets. Catalyst stability is implicitly accounted for by recording the target values at the end of the reaction or after every 10 h on stream (see below). We select 11 input features, comprising 5 process parameters and 6 catalyst properties, that could be relevant to the prediction of the

targets (Table 1), and later perform feature analyses to identify the features most relevant to target prediction. Our focus on catalyst properties that can be measured for any material, instead of more commonly employed structural, electronic, or compositional descriptors [27,29], maximizes the generality of our framework across catalyst architectures and formulations.

Our overall approach is illustrated in Fig. 1. We begin our data curation process by searching the Scopus database for all journal articles related to Ni-catalyzed DRM published within the past 20 years (search string shown in Supplementary Information Text S1). The search returned 1810 articles which were manually reviewed to exclude studies that did not report at least one complete data point (i.e., complete set of target properties and input features as described above). For instance, purely computational studies and studies with incomplete catalyst characterization were excluded from the dataset.

Table 1
Summary of features selected for machine learning model.

| Type | Features (Units) | Description |
|--------------------------|---|---|
| Process parameters | Ratio of CH ₄ in feed/CH ₄ feed fraction ^a | Ratio of volumetric flow rate of CH ₄ to the total volumetric flow rate of the feed to the catalytic reactor. Also equivalent to the CH ₄ partial pressure. |
| | Reaction temperature (°C) | Reaction temperature at which the DRM experiment was conducted. |
| | Nickel loading (%) ^b | Weight percentage of nickel present in the prepared catalyst. |
| | Reaction time (h) ^c | Reaction time at which the readings for conversions and syngas ratio are taken. |
| Catalyst characteristics | GHSV (ML/g _{cat} -h) ^d | Gas hourly space velocity of the reaction, defined as the total volumetric feed flow rate per unit mass of catalyst per hour. |
| | Pore size (nm) ^e | Pore diameter of the catalyst support. |
| | Pore Volume (cm ³ /g) ^e | Specific pore volume of the catalyst support. |
| | Surface Area (m ² /g) ^f | Specific surface area of the fresh catalyst. |
| | H ₂ -TPR peak temperature (°C) ^g | Temperature of maximum H ₂ uptake during temperature programmed reduction (TPR). |
| | Ni particle size (nm) ^h | Average diameter of Ni nanoparticles on the reduced catalysts. |
| | Modifier electronegativity ⁱ | The Pauling electronegativity of the modifiers, dopants, or promoters used in the catalyst preparation. |

a: The CH₄:CO₂ ratio was always equal to 1 across the entire dataset, while the diluent fraction in the feed differed.

b: Weight loadings determined by inductively coupled plasma (ICP) analysis were taken if reported, else the nominal weight loading was used.

c: The last data point was collected if time-on-stream data is available. For experiments exceeding 20 h, multiple data points from the time stream were taken at 10-hour intervals.

d: GHSV is calculated as follows: $\text{GHSV} \left(\text{ml g}_{\text{cat}}^{-1} \text{h}^{-1} \right) = \frac{\text{Feed Flow Rate} \left(\text{ml h}^{-1} \right)}{\text{Catalyst Weight} \left(\text{g}_{\text{cat}} \right)}$

e: Pore size and distributions are commonly measured using the Barrett-Joyner-Halenda (BJH) method, and author-reported average pore diameters and total pore volumes were taken.

f: Values taken were measured using Brunauer-Emmett-Teller (BET) analysis of N₂ physisorption data.

g: The largest peak was taken if multiple peaks were identified in the reduction profile.

h: Values taken were measured by transmission electron microscopy (TEM) if available, otherwise from x-ray diffraction (XRD) data using the Scherrer equation.

i: A weighted average value was taken if multiple modifiers were present in different amounts.

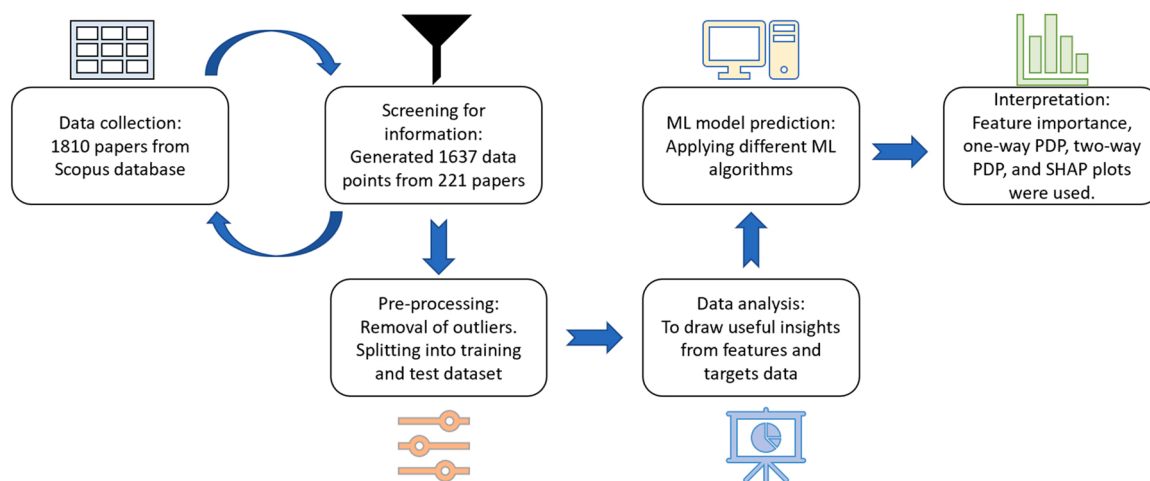


Fig. 1. : Schematic of our overall workflow indicating the data collection, pre-processing, and analysis followed by machine learning (ML) model application and its interpretation using feature importance plots, one-way and two-way partial dependence plots (PDPs), and Shapley Additive Explanations (SHAP) plots.

2.2. Data curation

In this work, we leveraged previously published data to bypass the many time-consuming experiments that would otherwise be required. Though the idea of automatically extracting the information through text mining may be promising [39,40], we observed that published studies on DRM often vary in terms of characterization techniques and experimental conditions, which may compromise the interpretability of the model [31]. Furthermore, data that is presented graphically (e.g., in a graph or figure) instead of textually (e.g., in a table) is often more difficult to automatically extract [41]. Therefore, instead of utilizing automated data retrieval methods, we manually scanned and extracted data from each article to reduce the erroneous data collection incurred by text mining methods. Where necessary, required numerical values from graphs presented in literature were extracted from figures using a graph reader tool. This procedure resulted in a smaller list of 221 papers (Supplementary Information Fig. S1), from which a total of 1637 complete data points were extracted by hand.

The NumPy [42] and pandas [43] software libraries in Python were used to prepare the data for visualization and model training. For predicting syngas ratio, outliers from the top and bottom 0.5 percentile of the target values for the prediction of syngas ratio are removed. These are extreme values and exceptional cases that have very few sample points and can therefore compromise the model accuracy. The top 0.5 percentile represents catalysts which produce syngas ratio above 1.3, which is significantly greater than the expected syngas ratio (less than 1) in a DRM process with RWGS as a side reaction. We discuss some reasons for syngas ratios greater than unity later in Section 3.1. Conversely, the bottom 0.5 percentile represents poor performing catalysts that produce syngas ratios between 0 and 0.15, demonstrating low, almost negligible, activity for DRM. In both cases, these points fall outside the sample space of active Ni catalysts that are of interest, and thus may be detrimental to our exploration of properties that lead to a close-to-unity syngas ratio. The points removed are indicated in Supplementary Information Table S1. Following the convention of the train-test split, the data set was randomly partitioned to assign 90% of data points to the train set and 10% to the test set. We provide further information on our machine learning workflow in the Appendix.

2.3. Model evaluation and data analysis

Our work evaluates three ensemble tree models, namely Random Forest (RF) [35], Gradient-Boosting Regressor (GBR) [36] and Categorical Boosted Regressor (CatBoost) [37]. We provide additional details on the implementation of the different models in the Appendix

(and an introduction to their algorithms in Text S2). The scikit-learn library [44] was used to apply the RF and the GBR models, and the CatBoost library for Python was used to apply the CatBoost Regressor. The model performance was evaluated using the default root-mean-square error (RMSE) criterion, and the model scores determined by the coefficient of determination value R^2 . For model testing, regression plots of the predicted target values against the actual target values were presented to illustrate the prediction performance of the trained model. The matplotlib library [45] was used for plotting histograms, scatter plots and other data visualization methods. The seaborn library [46] was also used to plot heatmaps of the correlation matrix for the features to visualize the correlation coefficient between the pairs of input features in our dataset. For model interpretation, line plots of one-way partial dependence plots (PDP) for each feature variable provided by the scikit-learn library were used to visualize the interaction between an input feature and the target response. Two-way PDPs were presented as three-dimensional (3D) surface plots to visualize the effects of a pair of input features on the target response [47]. The trajectory plots used to illustrate the effect of tuning each feature value on the partial dependence values on two target variables are obtained by first computing the partial dependence values from the trained models, then plotting the partial dependence values on a scatterplot with a colormap that illustrates the range of feature values. The points depicted constitute the 5th to the 95th percentiles in the dataset, with a lighter color representing a feature value that obtained lower percentile in the dataset and a darker color representing a feature value obtained at a higher percentile in the dataset.

2.4. Model Interpretation Techniques

After model training, we applied model interpretation tools to analyze and visualize the different effects of our feature inputs on the target responses. Feature importance can be computed based on three different methods, namely the Gini importance, permutation importance, and Shapley Additive exPlanations (SHAP) values [48]. Feature importance plots based on the first two methods (Gini importance and permutation importance) were provided by the scikit-learn library, while SHAP plots were implemented using the SHAP software library [49]. In particular, the bee swarm plot in the SHAP library was applied to visualize the importance of each feature to the model and how variance in each feature affects the model output. The Shapley value is based on fair allocation results from cooperative game theory to allocate importance or credit for a model's output to its input features, which ranks the impact of each feature on the trained model. Theoretical background on the computations of feature importance, permutation

importance and SHAP values are provided in [Supplementary Information](#) Text S3.

One-way and two-way PDPs implemented in the scikit-learn library were used to show the dependence between the target values and a set of input features of interest while keeping the values of the other features at their mean values. In other words, PDP is a method to visualize the marginal effect of a set of features on the predicted target response of a trained machine learning. The predicted impact of process parameters and catalyst properties on syngas ratio, CH₄ conversion and CO₂ conversion can be analyzed from the trends illustrated by PDP analysis. We also connect our observed trends observed in our PDPs to reasoning from the current literature in order to highlight the interpretability of our results.

3. Results and discussion

3.1. Data analysis and visualization

We begin our analysis by obtaining correlation coefficients between each pair of features to better understand our dataset. The heat map of the correlation matrix is shown in [Fig. 2a](#), in which a dark red hue represents a strong positive correlation coefficient, a dark blue hue represents a strong negative correlation coefficient, and a light-yellow hue represents a weak correlation coefficient. As is ideal for training ML models, most of the features possess weak cross-correlations, except

for (1) a strong positive correlation between surface area and pore volume, and (2) a moderate negative correlation between surface area and pore size. These correlations agree with what is generally understood about the textural properties of catalyst supports: highly porous materials with small pores tend to have larger specific surface areas arising from the interstitial voids within the pores. Although such multicollinearity can potentially underestimate the importance of correlated features [50], we nevertheless retained all features to avoid the potential loss of important information for model training.

The distributions of the raw data collected for our targets, namely CH₄ conversion, CO₂ conversion and syngas ratio, are shown in [Fig. 2b](#). Further, a summary of their descriptive statistics such as mean, median, standard deviation and skewness of each distribution is provided in [Supplementary Information Table S2](#). The reactant (i.e., CH₄ and CO₂) conversions within the dataset range from 0% to nearly 99% with average values of 59.9% and 67% respectively. The slightly higher conversions for CO₂ than CH₄ are consistent with CO₂ being consumed in multiple side reactions, such as RWGS and coke gasification, in addition to DRM. After the removal of outliers (see [Section 2.2](#)), the syngas ratio dataset has 1620 sample points with minimum, average and maximum values of 0.165, 0.827 and 1.29 respectively. Interestingly, syngas ratios of greater than 1 have been reported by a small minority of studies in apparent exception to the general rule of thumb that syngas ratios are typically less than 1 because of the parasitic H₂-consuming RWGS reaction. Two reasons, both involving other side reactions, have

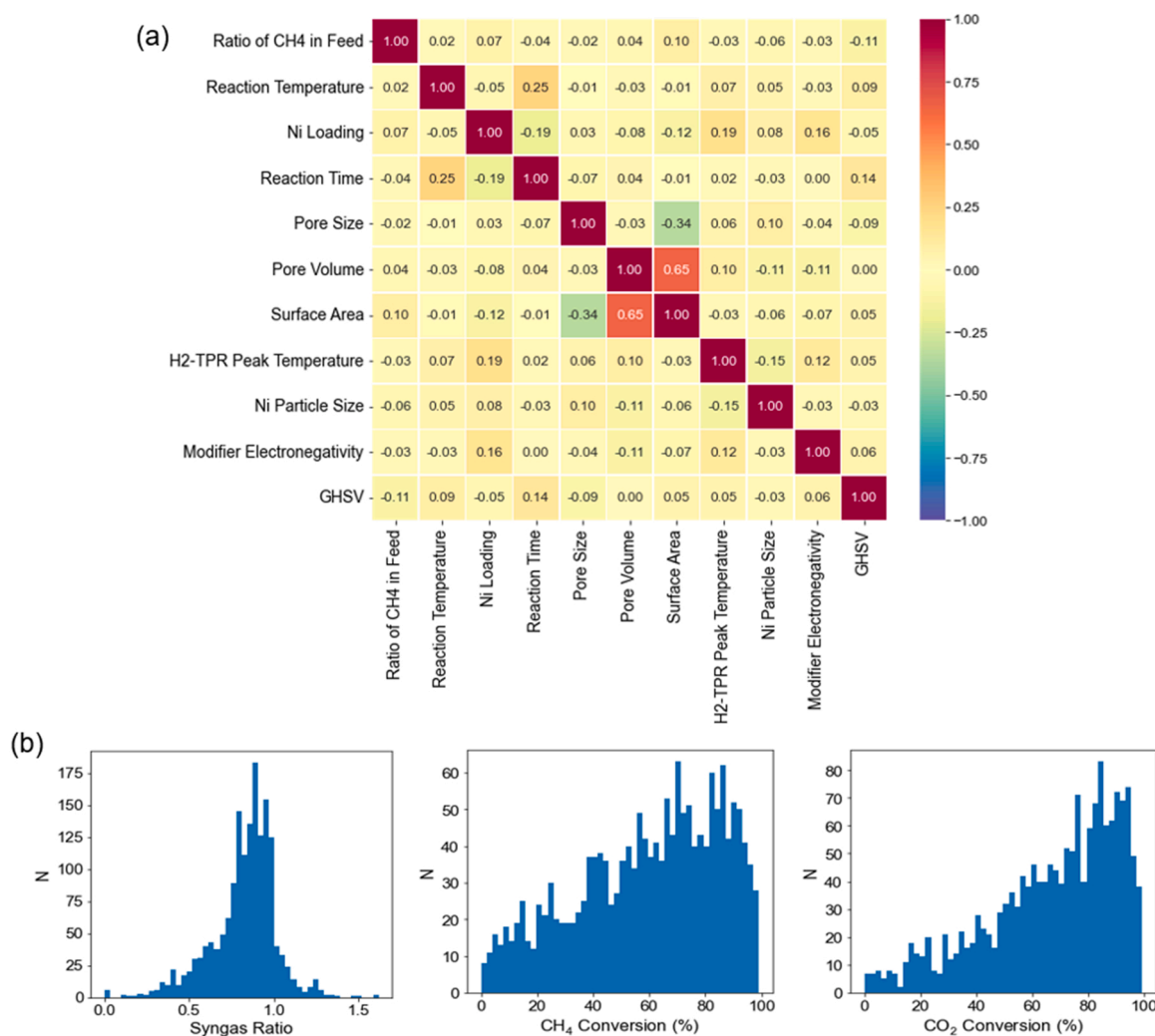


Fig. 2. : Overall properties of dataset. (a) Correlation matrix heat map displaying the correlation coefficients across each pair of features. (b) Distribution plots of target values: left – syngas ratio, center: CH₄ conversion, right: CO₂ conversion.

been proposed in the literature to explain these anomalously high syngas ratios. Firstly, the Boudouard reaction ($2\text{CO} \rightleftharpoons \text{CO}_2 + \text{C}$) may be favored under high CO concentrations, which will decrease the relative concentration of CO and thus increase the syngas ratio [51]. Secondly, catalysts that are particularly prone to direct methane decomposition ($\text{CH}_4 \rightleftharpoons 2\text{H}_2 + \text{C}$) will produce additional H_2 as a result of this side reaction [52]. Thus, although the possibility of producing syngas with

greater-than-unity H_2/CO ratio is nominally attractive, such behavior is invariably accompanied by significant carbon deposition, either by the Boudouard reaction or methane decomposition, that are highly detrimental to the overall DRM process.

It is also noteworthy that the distributions for conversions and syngas ratio are skewed towards the right, most likely pointing towards an inherent bias in the published literature against the reporting of poor-

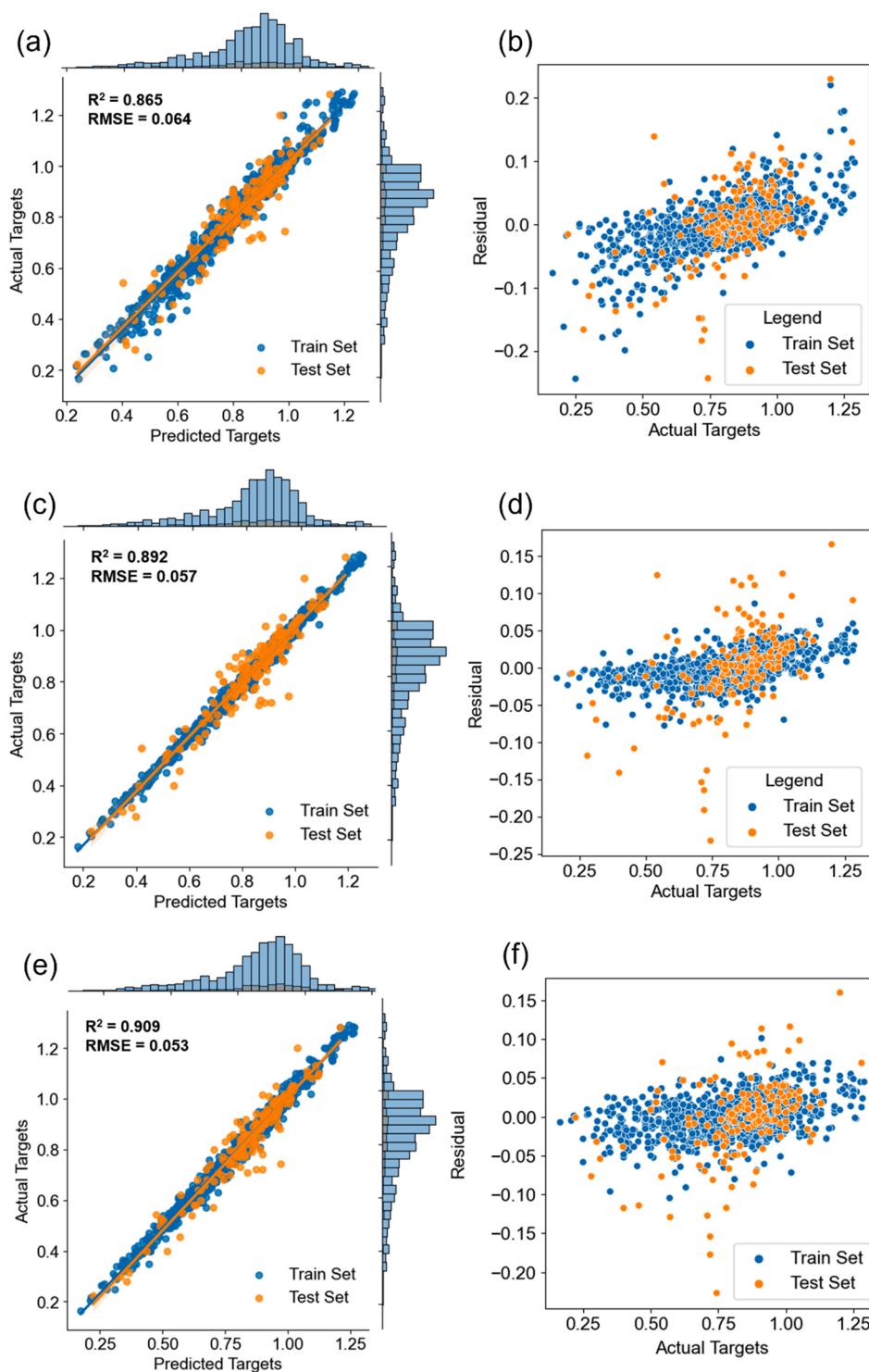


Fig. 3. : Regression plots (showing R^2 , RMSE and data distribution on gridlines) and residual distribution plots for the prediction of syngas ratios using: (a-b) random forest regressor, (c-d) gradient boosted regressor and (e-f) CatBoost regressor. Residuals are computed as the difference between the actual target and predicted target values.

performing catalysts that would give lower values. The skewness of feature distributions (see [Supplementary Information Fig. S2](#) and [Table S3](#)) can possibly also be explained by the same reason.

Finally, we also observe a moderate positive linear relationship between syngas ratio and reactant conversions (see [Supplementary Information Fig. S3](#)), with an adjusted R^2 of 0.46 and RMSE of 0.14 from a linear regression using syngas ratio as the dependent variable and reactant conversions as independent variables. This relationship can be explained by the common underlying effect of reaction temperature on each of these parameters if the RWGS steps are assumed to be fully equilibrated at varying DRM conversions, as previously demonstrated for Ni/SiO₂ catalysts [20] and confirmed by our own Aspen simulations (simulation details provided in Appendix; Table of results provides [Supplementary Information Table S4](#)). From the slope of the best-fit line, a 1% increase in average reactant conversion is accompanied by an increase of roughly 0.005 in syngas ratio. However, the relatively weak correlation motivates a closer examination of whether it is possible to identify features that affect syngas ratio independently of reaction conversions, which we return to in [Section 3.5](#).

3.2. Prediction of syngas ratio

We then train RF, GBR, and CatBoost models on the training set to predict the syngas ratio of the test set. The performance of each model is evaluated based on the coefficient of determination (model score; R^2) and RMSE between the actual and predicted syngas ratios. All three models demonstrate good R^2 values of 0.87–0.91, among which the CatBoost model exhibited the highest R^2 value of 0.91 and the lowest RMSE of 0.053 (see [Fig. 3](#)).

To determine the importance of different features in affecting syngas ratio, we perform a feature importance analysis using the SHAP bee swarm plots (see [Fig. 4](#)). The three most important features are reaction temperature, gas hourly space velocity (GHSV) and Ni particle size, which have the greatest variance in SHAP values as illustrated on the horizontal axis. The bee swarm plot also illustrates the expected effects of feature values (represented by the color hue of the points in [Fig. 4](#)) on the target SHAP value (as shown on the x-axis in [Fig. 4](#)). Particularly, a higher value of reaction temperature, as indicated by the “swarm” of points in pink, results in a higher SHAP value, and thus a higher predicted syngas ratio. The model predicts that a lower GHSV and smaller Ni particle size, illustrated by the clusters of points in dark blue in [Fig. 4](#), result in a higher SHAP value and predicted syngas ratio. Accordingly, higher values of surface area, Ni loading, pore volume, H₂-TPR peak temperature, pore size, and sum of 2 other features, result in a lower SHAP value and predicted syngas ratio.

temperature and pore size generally result in a higher predicted syngas ratio, whereas a higher CH₄ feed fraction results in the opposite. The effects of reaction time and modifier electronegativity are less significant on the SHAP values and are deemed to be least important. The feature importance determined by Gini importance and permutation importance (see [Supplementary Information Fig. S4](#)) are largely in agreement with our SHAP analysis.

3.3. Effect of process parameters on syngas ratio

Among the process parameters, the SHAP plots shown above (see [Fig. 4](#)) illustrate that temperature and GHSV have the most significant effects on the syngas ratio. High temperatures thermodynamically favor the strongly endothermic DRM reaction over the RWGS side reaction, thus leading to a higher syngas ratio, which is also observed in our partial dependence plots (PDPs) (see [Fig. 5a](#)) and confirmed by thermodynamic simulations in Aspen Plus (see [Supplementary Information Fig. S5](#)). However, if syngas ratio were fully determined by thermodynamics, then one would not expect to observe a change in syngas ratio with the GHSV, but the corresponding one-way PDP (see [Fig. 5b](#)) instead shows that the syngas ratio initially decreases with increasing GHSV before leveling off. Above a reaction temperature of ca. 800 °C, the model shows that syngas ratio does not change notably in value since the RWGS reaction is favored [16]. Such behavior is consistent with a reactions-in-series model in which the RWGS rate is dependent on the concentrations of the DRM products (i.e., H₂), and thus increases as the GHSV is reduced and overall conversions increase [53]. Additionally, syngas ratio decreases slightly as CH₄ feed fraction increases until a value of 0.3, and subsequently appears to level off (see [Fig. 5c](#)). Within our dataset, CH₄ feed fraction is a proxy for the extent of feed dilution (see [Table 1](#)) which, according to Le Chatelier's principle, should shift the equilibrium in favor of DRM while also hindering the forward RWGS reaction. Experimental results have also shown that lower CH₄ ratios in feed lead to a syngas ratio that is closer to unity [54]. The PDP of reaction time, which does not have a significant effect on syngas ratio, is depicted in [Supplementary Information Fig. S6](#). The negligible effect of reaction time, which is intended to capture the effect of deactivation, may be due to a bias against the publication of rapidly deactivating catalysts.

From two-way PDPs, we can draw useful interpretations of the effects of two features simultaneously on the syngas ratio (see [Fig. 6](#)). In particular, they definitively exclude the presence of confounding cross-correlation effects between each feature, and thus confirm our

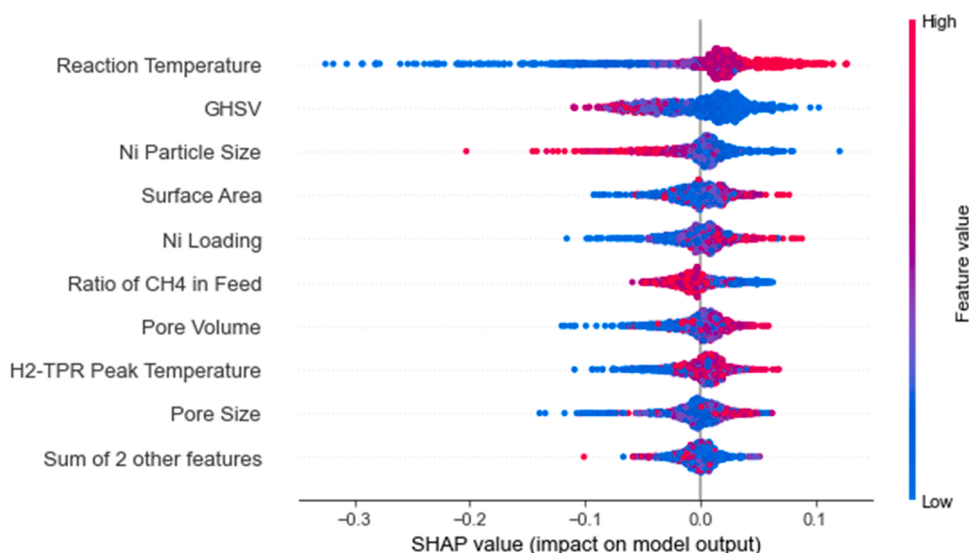


Fig. 4. : SHAP bee swarm plot showing feature importance for prediction of syngas ratio.

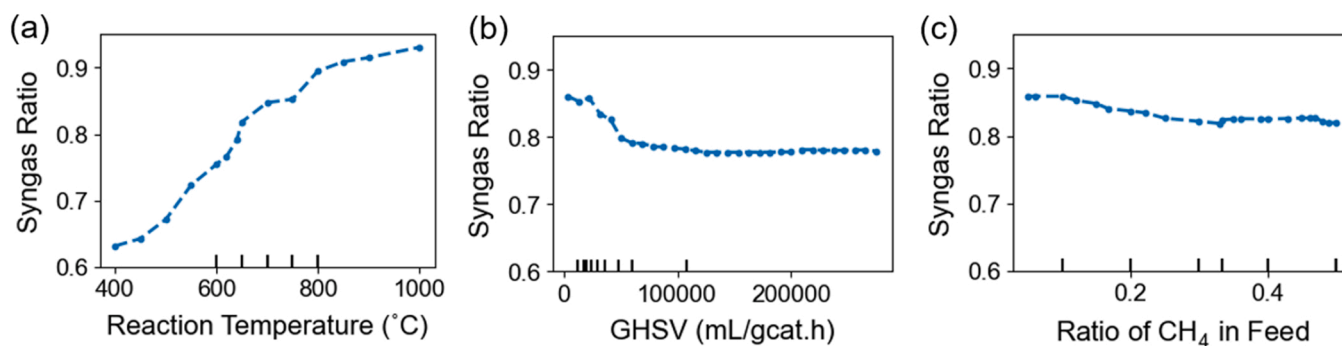


Fig. 5. : One-way partial dependence plots of the effects of process parameters on syngas ratio, constructed with feature values from the 1st to 99th percentile. The black lines on the x-axis indicate the approximate distributions of features in our dataset, where each line indicates a consecutive 10th percentile starting from the leftmost line (10th percentile) to the rightmost line (90th percentile).

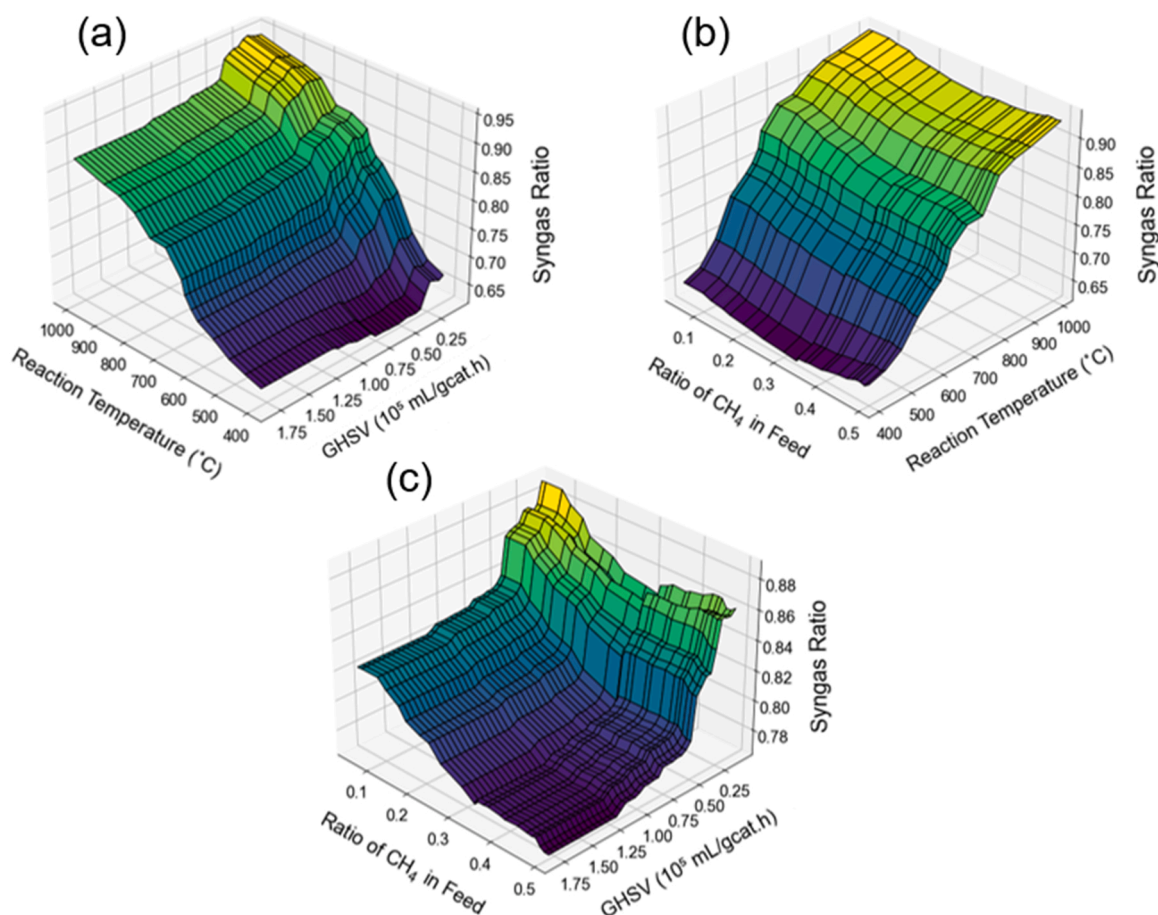


Fig. 6. : Two-way partial dependence plots of the effects of pairs of process parameters on syngas ratio: (a) Reaction temperature and GHSV, (b) CH₄ feed fraction and GHSV, and (c) CH₄ feed fraction and reaction temperature. The surfaces are colored according to their relative syngas ratio values (blue: low, yellow: high).

conclusions from the one-way PDPs that high syngas ratios are favored by lower GHSVs and increased feed dilution, which could serve as process handles for achieving close-to-unity syngas ratios.

3.4. Effect of catalyst parameters on syngas ratio

Among the catalyst design parameters investigated, Ni particle size has the most pronounced effect on the syngas ratio (see Fig. 7a) with a strong negative correlation between the syngas ratio and particle size. Two possible hypotheses can be put forth for this observation. Firstly, if the RWGS elementary steps are continuously equilibrated, then the

particle size may not directly affect the syngas ratio, instead exerting only an indirect influence through its effect on reactant conversions (see Section 3.5). In a study on low-temperature DRM over Ni/SiO₂ catalysts, Baudouin et al. observed that syngas ratio was largely governed by the CH₄ or CO₂ conversion independently of underlying particle size, which was attributed to competitive adsorption of DRM and RWGS intermediates on the Ni surface and consequent inability to decouple both processes [20]. While their findings are in agreement with several older studies [19,55], RWGS has sometimes also been found to be not in dynamic equilibrium [56]. Alternatively, if the DRM and RWGS reactions are catalyzed by different sites on the same catalyst whose relative

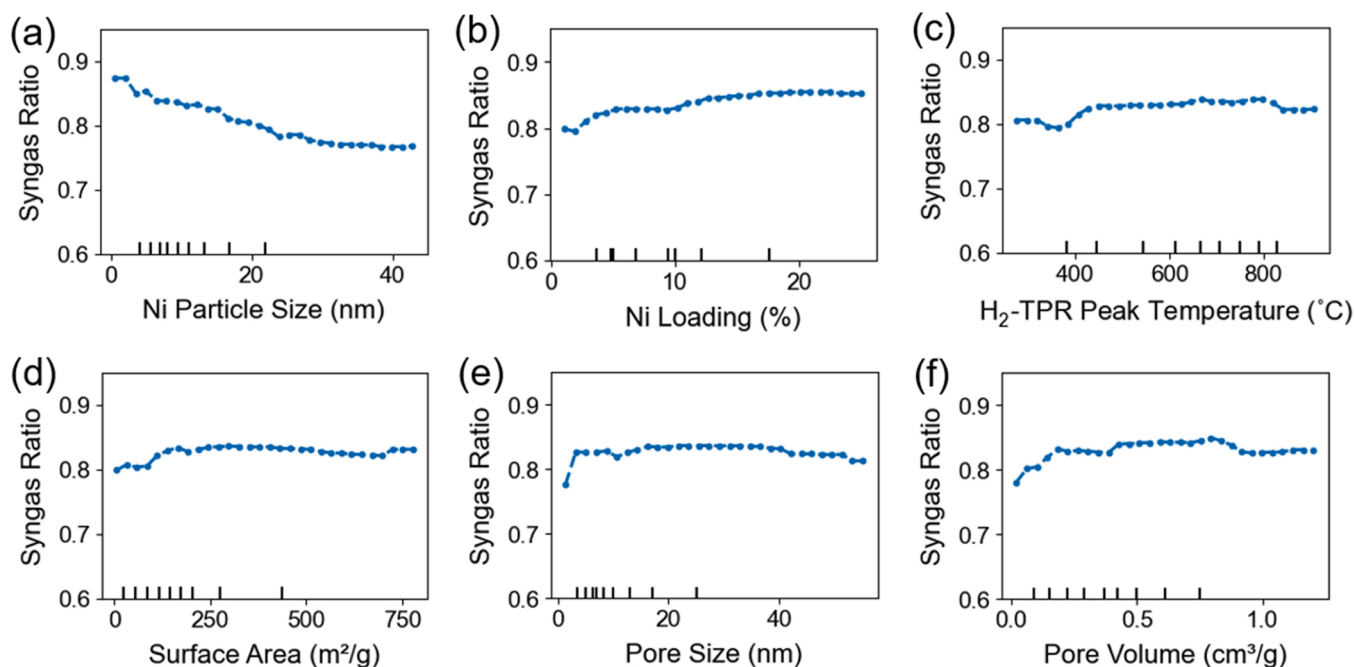


Fig. 7. : One-way partial dependence plots of the effects of catalyst parameters on syngas ratio, constructed with feature values from the 1st to 99th percentile. The black lines on the x-axis indicate the approximate distributions of features in our dataset, where each line indicates a consecutive 10th percentile starting from the leftmost line (10th percentile) to the rightmost line (90th percentile).

fractions are affected distinctly by particle size, then particle size can play a direct role in determining the relative selectivities towards DRM and RWGS, and hence the observed syngas ratio. For instance, Foppa et al. showed computationally and experimentally for Ni/Al₂O₃ that all surface Ni atoms are active for DRM, whereas only the Ni-Al₂O₃ interface sites are implicated in the forward water gas shift reaction [57]. The methane decomposition reaction (Section 3.1), which is particularly favorable over moderately-large Ni particles (ca. 20 – 100 nm) [58], may also increase observed syngas ratios beyond what is expected from the DRM/RWGS balance alone. Also, the nature of the support can influence the mechanisms, active sites and dominant surface intermediates: for instance, reducible metal oxides such as CeO₂ can induce a bifunctional mechanism involving lattice oxygen vacancies that enable the decoupling of CO₂ and CH₄ activation steps. [12].

To the best of our knowledge, there have not been any studies in the published literature that have elucidated the precise effect of metal nanoparticle size on syngas ratios over realistic DRM catalysts. Experimentally, it can be difficult to isolate the effect of particle size from that of other catalyst parameters while also keeping the conversion and extents of coking and sintering unchanged. To this end, the approach of Han et al., in which pre-synthesized Ni nanoparticles of different sizes are deposited onto an inert support and coated with different oxide overlayers to minimize coking and sintering [21], could be promising. On the other hand, first-principles computational studies are complicated by the need to calculate product yields at high reactant conversions to match experimental conditions, which would necessitate a full microkinetic model in addition to a realistic depiction of the working catalyst surface under reaction conditions, which can be challenging to obtain for complex catalyst architectures. Nevertheless, our present results suggest that such studies are warranted, and work along these lines is currently ongoing in our laboratory.

Interestingly, syngas ratio increases with Ni loading up to ca. 20 wt% Ni, above which the effect attenuates (see Fig. 7b). Though this trend may appear to contradict that observed for the particle size considering that particle sizes usually increase with Ni loadings, the one-way PDPs are obtained by varying one feature at a time while keeping the other features at their average values; in other words, they assume that the

features are decoupled from each other. Thus, our model points to a synergistic effect between higher Ni loadings and small particle sizes in achieving optimal syngas ratios, which is further confirmed by two-way PDPs (see Fig. 8a). In practice, high Ni loadings and small particle sizes can be simultaneously achieved by improving dispersions through tailored syntheses involving mesoporous supports in tandem with strong metal-support interactions [59].

Surprisingly, modifier electronegativity does not have a significant effect on syngas ratio (see Supplementary Information Fig. S6), even though the addition of promoters is a common strategy in catalyst design. There are two possible explanations for this observation. Firstly, the effects of promoters on textural properties, such as Ni dispersion and strength of metal-support interactions, could already have been captured by other catalyst features, namely H₂-temperature programmed reduction (TPR) peak temperature, surface area, and particle size. Secondly, despite its successful use as a descriptor in several studies [28,29], the electronegativity may be too simplistic of a descriptor for the promoter's effect on a catalyst, which could occur via diverse mechanisms such as enhancing redox properties or Brønsted/Lewis acidity/basicity. Unfortunately, the corresponding experimental measurables (e.g., band gap, oxygen vacancy density, titration, or temperature-programmed desorption results) are often only qualitatively reported in the literature and rarely quantified.

The temperature of maximum H₂ consumption during TPR is indicative of the reducibility of the catalyst, and in turn the strength of interactions between the unreduced oxide phase and the catalyst support. For Ni-based catalysts, peaks around ca. 300–400 °C are typically assigned to the bulk NiO weakly interacting with the support, 400–600 °C to the well-dispersed NiO strongly interacting with the support, and > 600 °C to the poorly reducible mixed oxide phases (e.g., silicates or aluminates). We observe that optimal syngas ratios are achieved between ca. 400 °C and 800 °C (see Fig. 7c). We hypothesize that the weak metal-support interactions of easily reducible NiO phases induce sintering under reaction conditions, leading to larger particle sizes. Conversely, poorly reducible precursors and overly strong metal-support interactions may result in a low degree of reduction and correspondingly an absence of Ni metal species for the reaction at lower

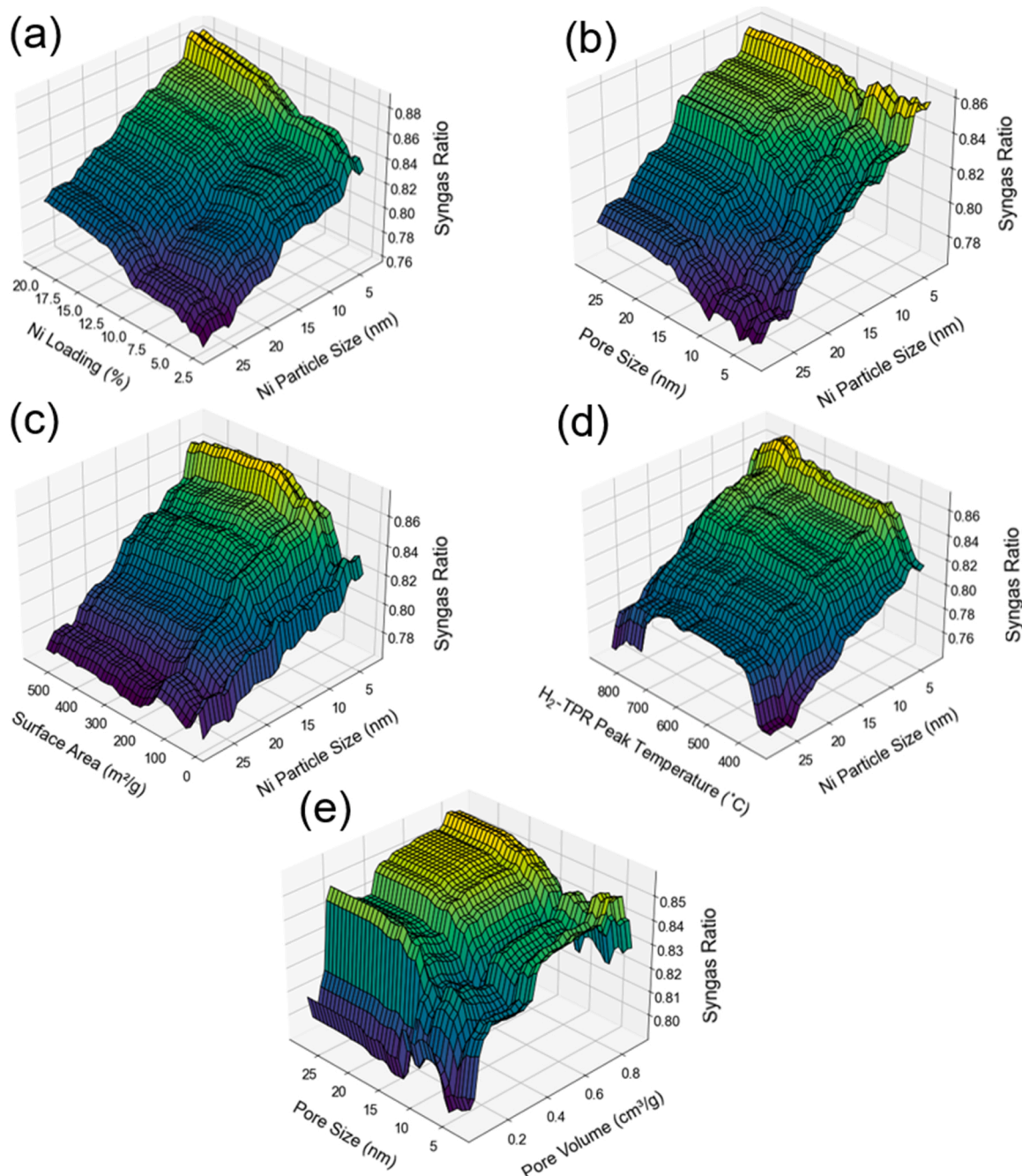


Fig. 8. : Two-way partial dependence plots of the effects of pairs of catalyst parameters on syngas ratio: (a) Ni loading and Ni particle size, (b) Pore size and Ni particle size, (c) Surface area and Ni particle size, (d) H₂-TPR peak temperature and Ni particle size, and (e) Pore size and pore volume. The surfaces are colored according to their relative syngas ratio values (blue: low, yellow: high).

reaction temperatures,[60] thus causing conversions and syngas ratios to decrease.

For textural properties, we observe that syngas ratio increases with surface area (see Fig. 7d), pore size (see Fig. 7e) and pore volume (see Fig. 7f) until critical values of ca. 400 m²/g, 40 nm, and 1 cm³/g respectively. The effects of pore volume and surface area, which are strongly correlated (see Fig. 2), can be attributed to increased Ni dispersion which indirectly favors smaller Ni particle sizes. The effect of pore size is subtler because it is usually difficult to introduce very small pores to common support materials such as mixed oxides, hydroxyapatite, and layered double hydroxides. Thus, the observed correlation between pore size and syngas ratio may not imply causation and is more likely because the best-performing supports for achieving high syngas

ratios are difficult to synthesize with very small pore sizes.

Finally, the remainder of the two-way PDPs illustrating the effect of catalyst parameters on syngas ratio are shown in Fig. 8b-d. These plots together show that the preference for a smaller particle size dominates the determination of syngas ratio, with the other catalyst parameters playing relatively minor roles.

3.5. Decoupling syngas ratios and reactant conversions

The same process used for the prediction of syngas ratio is used to train a tree regressor model to predict CH₄ and CO₂ conversions. The CatBoost model demonstrates good prediction accuracy with test scores (R²) of 0.895 and 0.875 for CH₄ and CO₂ conversions, as shown by the

regression plots in [Supplementary Information Fig. S7](#). SHAP plots are again used to evaluate the feature importance for predicting CH₄ and CO₂ conversions (see [Supplementary Information Fig. S8](#)), and show that process parameters, particularly reaction temperature, GHSV and CH₄ feed fraction, are the most important features for predicting both CH₄ and CO₂ conversions. However, catalyst properties such as pore volume, H₂-TPR peak temperature, Ni particle size, surface area, and pore size are also of mild importance for predicting conversions, in agreement with the relevance of catalyst design for achieving high reactant conversions in DRM.

As discussed in [Section 3.1](#) above, considering the moderate correlation between syngas ratio and reactant conversions in our dataset, we focus only on identifying where the effects of each feature on reactant conversions and syngas ratio diverge. The one-way PDPs of the effects of each feature on reactant conversions are shown in [Supplementary Information Fig. S9-S10](#), and two-way PDPs for important feature pairs are provided in [Supplementary Information Fig. S11-S14](#). To visualize each feature's simultaneous effect on conversion and syngas ratio, we plot the PDP-predicted CH₄ conversions and syngas ratios across the range of feature values on the same axes (see [Fig. 9](#)). The corresponding plots for CO₂ conversion are very similar and presented in [Supplementary Information Fig. S15](#). In this manner, each feature's contribution to the overall positive correlation between syngas ratio and conversion can be decoupled and compared independently.

With several exceptions, the predicted syngas ratios and CH₄ conversions are strongly correlated across most features, with slopes that are in general agreement with the overall trend (i.e., a ca. 0.005 unit increase in syngas ratio per 1% increase in CH₄ conversion). The Ni particle size and Ni loading exert much stronger effects on syngas ratio

than on CH₄ conversion. By varying Ni particle size across the 5th to the 95th percentile of the dataset (ca. 3–26 nm) while holding all other features constant at their average values, the predicted syngas ratio decreases by ca. 0.011 units for every 1% decrease in the predicted CH₄ conversion. Similarly, the predicted syngas ratio increases from ca. 0.82–0.85 as Ni loading increases from ca. 3–20%, while the predicted CH₄ conversion remains almost unchanged (ca. 61%) across the same range of Ni loadings. These PDP correlation analyses are corroborated by the SHAP plots (see [Fig. 4](#) and [Supplementary Information Fig. S8](#)), which show Ni particle size and Ni loading as the 3rd and 5th most important features respectively for predicting syngas ratio, but only the 5th and 9th most important features for predicting CH₄ conversion. In contrast, pore size affects reactant conversions more strongly than syngas ratio: for pore sizes between ca. 4 and 27 nm, the predicted CH₄ conversion varies between ca. 55% and 62% while the predicted syngas ratio remains nearly constant (ca. 0.83). Overall, our observations highlight the possibility of designing catalysts, using the metal loading, particle size, and pore size as potential handles, to tune product syngas ratios at any reactant conversion.

The low importance of Ni loading in predicting conversions may be particularly surprising considering that, all else being equal as assumed in the PDP analysis, increasing the metal content should increase the number of active sites for the DRM reaction. We believe that this could be a result of the current trend in the published literature towards highly-dispersed, single-atom catalysts [\[61\]](#) that demonstrate excellent DRM activity at relatively low Ni loadings. Our study nevertheless points to an independent positive effect of Ni loading on syngas ratio, which could motivate future global optimization studies [\[62\]](#) that take into account tradeoffs between the synthetic accessibilities of multiple

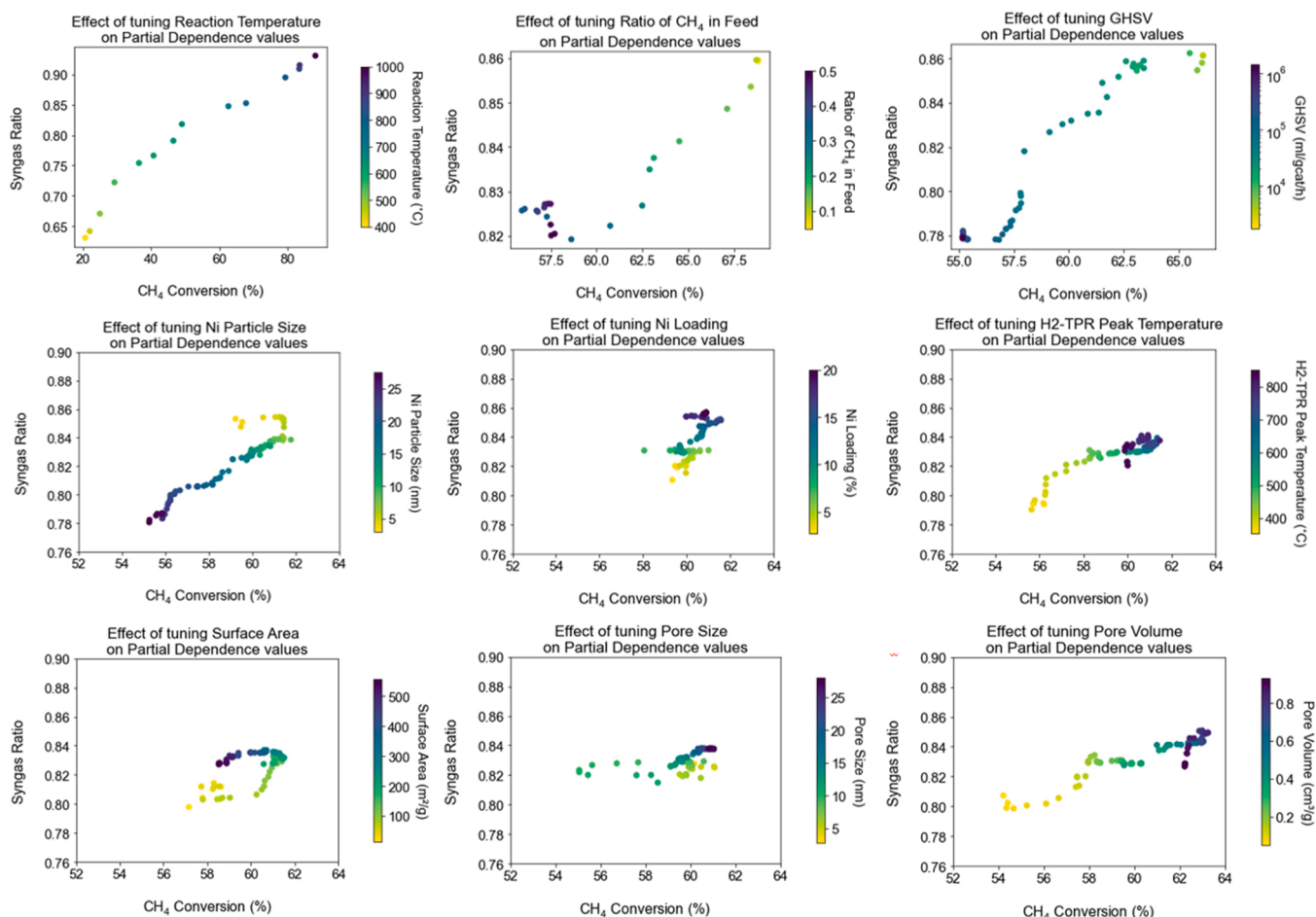


Fig. 9. : Trajectory plots showing each process and catalyst parameter's simultaneous effect on syngas ratio and CH₄ conversion.

design criteria.

4. Conclusions

In this work, we performed an exploratory interpretable ML analysis, trained on a comprehensive dataset curated from recent literature, of the effects of process parameters and catalyst properties on reactant conversions and syngas ratios in Ni-catalyzed DRM. By applying posteriori interpretation methods to the black-box ML model results, we were first able to reproduce basic trends concerning process parameters that are in accordance with overall thermodynamic analysis of the DRM process: higher syngas ratios are favored by higher reaction temperatures, lower GHSVs and dilute feeds.

In terms of catalyst parameters, we observed that the preference for a smaller Ni particle size is the primary determinant of high syngas ratios. Furthermore, syngas ratio and reactant conversions are moderately correlated and the residual variance can largely be attributed to the divergent effects of Ni particle size and Ni loading: while syngas ratio decreases with Ni particle size and increases with Ni loading, their corresponding effects on reactant conversions are far more muted. Thus, in contrast to previous studies on silica-supported catalysts concluding that syngas ratio is thermodynamically controlled, our present results that were derived over a comprehensive dataset covering diverse catalyst formulations and morphologies suggest that the RWGS and DRM reactions can be partially decoupled. Our findings also suggest the possibility of designing catalysts, using the metal loading, particle size, and pore size as potential handles, that are particularly selective for DRM and able to achieve high product syngas ratios at any reactant conversion: in particular, our model suggests a combination of smaller particle sizes, higher metal loadings and, to a lesser extent, larger pore sizes to be beneficial in this regard. At the same time, our exploratory study also highlights the potential of data-driven ML models to complement experimental and theoretical studies in heterogeneous catalysis by uncovering structure-property relationships that can then be investigated in greater detail. Crucially, these models facilitate the isolation of the individual effects of the various design parameters, which would otherwise be difficult to observe in experimental studies. Subsequently, we also anticipate extending our study to predicting optimal DRM catalyst formulations by applying global optimization methods that simultaneously consider material synthesizability in addition to the effects of different features on target values, and leveraging our dataset and similar datasets as training sets for the development of automated text mining approaches tailored towards the heterogeneous catalysis literature.

The limitations of our model are primarily related to the bias of published data towards high-performing catalysts, which results in a relatively sparse traversal of feature space that is not conducive to ML model training. Understandably, this bias limits the model from interpreting the effect of the feature over the entire range of its values,

especially at the tail ends of the feature and target distributions. Therefore, though the overall trend and the general understanding of feature effect may hold true, the accuracy of model interpretation techniques may be less reliable for those ranges of feature or target values. Further limitations include the inability of electronegativity as a sole descriptor to fully capture the electronic effects exerted by catalyst promoters, and the limited generalizability of the PDP trends in a large general catalyst dataset to a specific smaller subset of catalyst data due to the Simpson's paradox – in which a trend is observed in several subsets of data but the reverse trend is observed for the general dataset [63]. Future work will focus on addressing these limitations by incorporating a well-designed high-throughput experimental dataset to supplement the sparsely traversed regions of our model, and identifying improved descriptors for heteroatom promoters that can better describe the interactions between promoter and active metal.

CRediT authorship contribution statement

Keerthana Vellayappan: Conceptualization, Methodology, Investigation, Software, Validation, Writing – original draft, Visualization. **Yifei Yue:** Conceptualization, Methodology, Investigation, Software, Validation, Writing – original draft, Visualization. **Kang Hui Lim:** Conceptualization, Investigation, Validation, Writing – review & editing, Visualization. **Keyu Cao:** Data acquisition. **Ji Yang Tan:** Data acquisition. **Shuwen Cheng:** Data acquisition. **Tianchang Wang:** Data acquisition. **Terry Z.H. Gani:** Supervision, Writing – review & editing. **Iftekhar A. Karimi:** Supervision, Writing – review & editing, Funding acquisition. **Sibudjing Kawi:** Supervision, Writing – review & editing, Funding acquisition.

Declaration of Competing Interest

The authors declare that they have no known competing financial interests or personal relationships that could have appeared to influence the work reported in this paper.

Data Availability

Complete dataset and code are available on GitHub (<https://github.com/yifei-1021/DRM-ML-Project>).

Acknowledgment

This work was supported by A*STAR LCERFI (WBS: A-8000278–00-00) and FRC MOE T1 Project (WBS: A-0009184–00-00). Y.Y., K.H.L., K.C., J.Y.T. and T.W. acknowledge financial support from the National University of Singapore for their studies. S.C. acknowledges financial support from the China Scholarship Council.

Appendix: Model Details

Data and code availability

Complete dataset and code are available on GitHub (<https://github.com/yifei-1021/DRM-ML-Project>) upon acceptance of the manuscript.

Machine learning algorithms

The main types of machine learning algorithms that we considered are ensemble models, which combine the predictions made by multiple base estimators, particularly decision trees, to improve the overall generalizability and accuracy of the ensemble over a single estimator [64]. In this work, we adopted tree-based ensemble as decision trees are able to learn trends in complex and non-smooth feature space by partitioning the feature space into smaller subsets, which offers higher performance compared to simpler models such as logistic regression [65]. Compared to more popular deep

learning models, such as Multi-Layer Perceptions (MLPs), ensemble models often perform better for tabular data [66]: unlike MLPs, tree-ensemble models do not exhibit bias towards non-smooth target functions, and tree-ensemble models are more robust to uninformative and colinear features [66,67]. In addition, tree-based ensemble models are easier to implement and tune (e.g., ensemble trees allow the feature to be directly used as inputs to the ensemble model without the need for normalization):

Tree-based ensemble models use two main ensemble methods, particularly bagging and boosting. In bagging, each decision tree in the ensemble is trained using a randomly sampled subset of the training dataset. In gradient boosting, the base decision trees in the ensemble are sequentially fitted with another decision tree to resolve inaccurate predictions produced by the previous decision tree [68]. Further details on the RF, GBR, and CatBoost algorithms are provided in [Supplementary Information Text S2](#), and the hyperparameters of each ensemble tree model are provided in [Supplementary Information Table S5](#).

Machine learning workflow

Our machine learning workflow is detailed as follows: (1) We performed the train-test split once (90%–10% train-test). (2) We used grid cross validation on the training set to find the optimal hyperparameters. (3) The model is trained on the training set that is partitioned at the start. (4) Model performance is evaluated and compared based on the test set.

Aspen plus thermodynamic simulations

Thermodynamic equilibrium calculations of dry reforming of methane (DRM) at any given temperature (i.e., 500°C–800 °C) and at atmospheric pressure (i.e., 1 bar) are based on minimizing the Gibbs free energy of a multicomponent system. The overall system is assumed to contain the main DRM reaction (i.e., $\text{CH}_4 + \text{CO}_2 \rightleftharpoons 2 \text{H}_2 + 2\text{CO}$) and its most prominent side reaction, the reverse water gas shift (RWGS, i.e., $\text{H}_2 + \text{CO}_2 \rightleftharpoons \text{H}_2\text{O} + \text{CO}$). The total Gibbs free energy (G^{total}) of the overall chemical system is the sum of the chemical potential of each species involved (i.e., CH_4 , CO_2 , H_2 , CO , H_2O and He, which is used as a diluent):

$$G^{\text{total}} = \sum_{i=1}^N n_i \mu_i \quad (1)$$

where n_i is the number of moles of species i and μ_i is the corresponding chemical potential of species i . The chemical potential can be defined as:

$$\mu_i = \Delta G_{f,i}^0 + RT \ln \left(y_i \hat{\phi}_i \frac{P}{P_0} \right) \quad (2)$$

where $\Delta G_{f,i}^0$ is the standard Gibbs free energy of formation for species i at standard conditions. R is the molar gas constant, T is the temperature, y_i is the molar fraction of species i , $\hat{\phi}_i$ is the fugacity coefficient of species i , P is the operating pressure, and P_0 is the pressure at standard conditions. The fugacity coefficient, $\hat{\phi}_i$, can be estimated from equation of state modelling in the gas phase. Based on Carlson's decision tree for equations of state selection, the Peng-Robinson Equation of State is the optimal choice for estimating fugacity coefficients in non-polar chemical systems, and hence chosen in our thermodynamics calculations [69]. The analysis was performed on Aspen Plus V12 using RGibbs reactor.

The same model was used for thermodynamic simulations with varying extents of DRM reaction at different temperatures to determine the syngas ratio trend. A conversion reactor was used to specify the extent of the reaction, and a Gibbs equilibrium reactor for RWGS was used to ensure RWGS is at equilibrium conversion. The simulated feed was an undiluted equimolar mixture of CH_4 and CO_2 at a pressure of 1 bar.

Associated content

Supplementary Information

Search string used in Scopus, theoretical background of models used, additional data visualization plots, tables of descriptive statistics, list of outliers, ML model hyperparameters (PDF).

Appendix A. Supporting information

Supplementary data associated with this article can be found in the online version at [doi:10.1016/j.apcatb.2023.122593](https://doi.org/10.1016/j.apcatb.2023.122593).

References

- [1] J. Rogelj, G. Luderer, R.C. Pietzcker, E. Kriegler, M. Schaeffer, V. Krey, K. Riahi, Energy system transformations for limiting end-of-century warming to below 1.5 °C, *Nat. Clim. Change* 5 (2015) 519–527.
- [2] S. Cheng, Z. Sun, K.H. Lim, T.Z.H. Gani, T. Zhang, Y. Wang, H. Yin, K. Liu, H. Guo, T. Du, L. Liu, G.K. Li, Z. Yin, S. Kawi, Emerging strategies for CO_2 photoreduction to CH_4 : from experimental to data-driven design, *Adv. Energy Mater.* 12 (2022) 2200389.
- [3] Y. Song, E. Ozdemir, S. Ramesh, A. Adishev, S. Subramanian, A. Harale, M. Albuali, B.A. Fadhel, A. Jamal, D. Moon, S.H. Choi, C.T. Yavuz, Dry reforming of methane by stable Ni-Mo nanocatalysts on single-crystalline MgO , *Science* 367 (2020) 777–781.
- [4] K. Wittich, M. Krämer, N. Bottke, S.A. Schunk, Catalytic dry reforming of methane: Insights from model systems, *ChemCatChem* 12 (2020) 2130–2147.
- [5] I.V. Yentekakis, P. Panagiotopoulou, G. Artemakis, A review of recent efforts to promote dry reforming of methane (DRM) to syngas production via bimetallic catalyst formulations, *Appl. Catal. B* (2021), 120210.
- [6] S. Lögdberg, D. Tristantini, Ø. Borg, L. Ilver, B. Gevert, S. Järås, E.A. Blekkan, A. Holmen, Hydrocarbon production via Fischer–Tropsch synthesis from H_2 -poor syngas over different Fe-Co/ γ - Al_2O_3 bimetallic catalysts, *Appl. Catal. B* 89 (2009) 167–182.
- [7] S. Damyanova, B. Pawelec, K. Arishtirova, M.V.M. Huerta, J.L.G. Fierro, The effect of CeO_2 on the surface and catalytic properties of Pt/ CeO_2 - ZrO_2 catalysts for methane dry reforming, *Appl. Catal. B* 89 (2009) 149–159.
- [8] I.V. Yentekakis, G. Goula, M. Hatzisymeon, I. Betsi-Argyropoulou, G. Botzoulaki, K. Kousi, D.I. Kondarides, M.J. Taylor, C.M. Parlett, A. Osatiashtiani, Effect of support oxygen storage capacity on the catalytic performance of Rh nanoparticles for CO_2 reforming of methane, *Appl. Catal. B* 243 (2019) 490–501.
- [9] W. Kong, Y. Fu, L. Shi, S. Li, E. Vovk, X. Zhou, R. Si, B. Pan, C. Yuan, S. Li, Nickel nanoparticles with interfacial confinement mimic noble metal catalyst in methane dry reforming, *Appl. Catal. B* 285 (2021), 119837.
- [10] A.L.A. Marinho, R.C. Rabelo-Neto, F. Epron, N. Bion, F.S. Toniolo, F.B. Noronha, Embedded Ni nanoparticles in CeZrO_2 as stable catalyst for dry reforming of methane, *Appl. Catal. B* 268 (2020), 118387.

- [11] Y. Liu, Y. Chen, Z. Gao, X. Zhang, L. Zhang, M. Wang, B. Chen, Y. Diao, Y. Li, D. Xiao, X. Wang, D. Ma, C. Shi, Embedding high loading and uniform Ni nanoparticles into silicalite-1 zeolite for dry reforming of methane, *Appl. Catal. B* 307 (2022), 121202.
- [12] S. Das, J. Ashok, Z. Bian, N. Dewangan, M.H. Wai, Y. Du, A. Borgna, K. Hidayat, S. Kawi, Silica-Ceria sandwiched Ni core-shell catalyst for low temperature dry reforming of biogas: Coke resistance and mechanistic insights, *Appl. Catal. B* 230 (2018) 220–236.
- [13] S. Das, A. Jangam, S. Jayaprakash, S. Xi, K. Hidayat, K. Tomishige, S. Kawi, Role of lattice oxygen in methane activation on Ni-phylosilicate@ Ce1-xZrxO2 core-shell catalyst for methane dry reforming: Zr doping effect, mechanism, and kinetic study, *Appl. Catal. B* 290 (2021), 119998.
- [14] J. Zhang, F. Li, Coke-resistant Ni@SiO₂ catalyst for dry reforming of methane, *Appl. Catal. B* 176 (2015) 513–521.
- [15] K. Mondal, S. Sasmal, S. Badgandi, D.R. Chowdhury, V. Nair, Dry reforming of methane to syngas: a potential alternative process for value added chemicals—a techno-economic perspective, *Environ. Sci. Pollut. R.* 23 (2016) 22267–22273.
- [16] F.G.M. de Medeiros, F.W.B. Lopes, B. Rego de Vasconcelos, Prospects and technical challenges in hydrogen production through dry reforming of methane, *Catalysts* 12 (2022) 363.
- [17] R.Y. Chein, Y.C. Chen, C.T. Yu, J.N. Chung, Thermodynamic analysis of dry reforming of CH₄ with CO₂, *High. Press., J. Nat. Gas. Eng.* 26 (2015) 617–629.
- [18] P. Cao, S. Adegbite, T. Wu, Thermodynamic equilibrium analysis of CO₂ reforming of methane: elimination of carbon deposition and adjustment of H₂/CO ratio, *Energy Procedia* 105 (2017) 1864–1869.
- [19] H. Swaan, V. Kroll, G. Martin, C. Mirodatos, Deactivation of supported nickel catalysts during the reforming of methane by carbon dioxide, *Catal. Today* 21 (1994) 571–578.
- [20] D. Baudouin, U. Rodemerck, F. Krumeich, A. De Mallmann, K.C. Szeto, H. Ménard, L. Veyre, J.-P. Candy, P.B. Webb, C. Thieuleux, Particle size effect in the low temperature reforming of methane by carbon dioxide on silica-supported Ni nanoparticles, *J. Catal.* 297 (2013) 27–34.
- [21] J.W. Han, J.S. Park, M.S. Choi, H. Lee, Uncoupling the size and support effects of Ni catalysts for dry reforming of methane, *Appl. Catal. B* 203 (2017) 625–632.
- [22] S.M. Moosavi, K.M. Jablonka, B. Smit, The role of machine learning in the understanding and design of materials, *J. Am. Chem. Soc.* 142 (2020) 20273–20287.
- [23] P. Schlexer Lamoureux, K.T. Winther, J.A. Garrido Torres, V. Streibel, M. Zhao, M. Bajdich, F. Abild-Pedersen, T. Bligaard, Machine learning for computational heterogeneous catalysis, *ChemCatChem* 11 (2019) 3581–3601.
- [24] A. Mazheika, Y.-G. Wang, R. Valero, F. Viñes, F. Illas, L.M. Ghiringhelli, S. V. Levchenko, M. Scheffler, Artificial-intelligence-driven discovery of catalyst genes with application to CO₂ activation on semiconductor oxides, *Nat. Commun.* 13 (2022) 419.
- [25] Z.W. Ulissi, A.J. Medford, T. Bligaard, J.K. Nørskov, To address surface reaction network complexity using scaling relations machine learning and DFT calculations, *Nat. Commun.* 8 (2017) 1–7.
- [26] M.E. Günay, R. Yildirim, Knowledge extraction from catalysis of the past: a case of selective CO oxidation over noble metal catalysts between 2000 and 2012, *ChemCatChem* 5 (2013) 1395–1406.
- [27] A. Smith, A. Keane, J.A. Dumesic, G.W. Huber, V.M. Zavala, A machine learning framework for the analysis and prediction of catalytic activity from experimental data, *Appl. Catal. B* 263 (2020), 118257.
- [28] M. Suvarna, T.P. Araújo, J. Pérez-Ramírez, A generalized machine learning framework to predict the space-time yield of methanol from thermocatalytic CO₂ hydrogenation, *Appl. Catal. B* (2022), 121530.
- [29] L. Foppa, C. Sutton, L.M. Ghiringhelli, S. De, P. Löser, S.A. Schunk, A. Schäfer, M. Scheffler, Learning design rules for selective oxidation catalysts from high-throughput experimentation and artificial intelligence, *ACS Catal.* 12 (2022) 2223–2232.
- [30] T.N. Nguyen, T.T.P. Nhat, K. Takimoto, A. Thakur, S. Nishimura, J. Ohyama, I. Miyazato, L. Takahashi, J. Fujima, K. Takahashi, T. Taniike, High-throughput experimentation and catalyst informatics for oxidative coupling of methane, *ACS Catal.* 10 (2020) 921–932.
- [31] J.A. Esterhuizen, B.R. Goldsmith, S. Linic, Interpretable machine learning for knowledge generation in heterogeneous catalysis, *Nat. Catal.* 5 (2022) 175–184.
- [32] B. Weng, Z. Song, R. Zhu, Q. Yan, Q. Sun, C.G. Grice, Y. Yan, W.-J. Yin, Simple descriptor derived from symbolic regression accelerating the discovery of new perovskite catalysts, *Nat. Commun.* 11 (2020) 3513.
- [33] W. Xu, M. Andersen, K. Reuter, Data-driven descriptor engineering and refined scaling relations for predicting transition metal oxide reactivity, *ACS Catal.* 11 (2021) 734–742.
- [34] X. Wang, S. Jiang, W. Hu, S. Ye, T. Wang, F. Wu, L. Yang, X. Li, G. Zhang, X. Chen, Quantitatively determining surface-adsorbate properties from vibrational spectroscopy with interpretable machine learning, *J. Am. Chem. Soc.* 144 (2022) 16069–16076.
- [35] L. Breiman, Random forests, *Mach. Learn.* 45 (2001) 5–32.
- [36] J.H. Friedman, Greedy function approximation: a gradient boosting machine, *Ann. Stat.* (2001) 1189–1232.
- [37] L. Prokhorenkova, G. Gusev, A. Vorobev, A.V. Dorogush, A. Gulin, CatBoost: unbiased boosting with categorical features, *Adv. Neural Inf. Process. Syst.* 31 (2018).
- [38] M. Christoph, Interpretable machine learning: A guide for making black box models explainable, 2019.
- [39] A.J. Medford, M.R. Kunz, S.M. Ewing, T. Borders, R. Fushimi, Extracting knowledge from data through catalysis informatics, *ACS Catal.* 8 (2018) 7403–7429.
- [40] Z. Jensen, E. Kim, S. Kwon, T.Z.H. Gani, Y. Román-Leshkov, M. Moliner, A. Corma, E. Olivetti, A machine learning approach to zeolite synthesis enabled by automatic literature data extraction, *ACS Cent. Sci.* 5 (2019) 892–899.
- [41] S. Park, B. Kim, S. Choi, P.G. Boyd, B. Smit, J. Kim, Text mining metal-organic framework papers, *J. Chem. Inf. Model* 58 (2018) 244–251.
- [42] C.R. Harris, K.J. Millman, S.J. Van Der Walt, R. Gommers, P. Virtanen, D. Cournapeau, E. Wieser, J. Taylor, S. Berg, N.J. Smith, Array programming with NumPy, *Nature* 585 (2020) 357–362.
- [43] W. McKinney, Data structures for statistical computing in python, *Proc. 9th Python Sci. Conf. Austin, TX* (2010) 51–56.
- [44] F. Pedregosa, G. Varoquaux, A. Gramfort, V. Michel, B. Thirion, O. Grisel, M. Blondel, P. Prettenhofer, R. Weiss, V. Dubourg, Scikit-learn: Machine learning in Python, *J. Mach. Learn. Res.* 12 (2011) 2825–2830.
- [45] J.D. Hunter, Matplotlib: A 2D graphics environment, *Comput. Sci. Eng.* 9 (2007) 90–95.
- [46] M.L. Waskom, Seaborn: statistical data visualization, *J. Open Source Softw.* 6 (2021) 3021.
- [47] T. Hastie, R. Tibshirani, J.H. Friedman, J.H. Friedman, The elements of statistical learning: data mining, inference, and prediction, Springer, 2009.
- [48] Y. Nohara, K. Matsumoto, H. Soejima, N. Nakashima, Explanation of machine learning models using improved Shapley Additive Explanation, *Proc. 10th ACM Int. Conf. Bioinforma. Comput. Biol. Health Inform.* (2019), pp. 546–546.
- [49] S.M. Lundberg, S.-I. Lee, A unified approach to interpreting model predictions, *Adv. Neural Inf. Process. Syst.* 30 (2017).
- [50] J.Y.-L. Chan, S.M.H. Leow, K.T. Bea, W.K. Cheng, S.W. Phooong, Z.-W. Hong, Y.-L. Chen, Mitigating the multicollinearity problem and its machine learning approach: a review, *Mathematics* 10 (2022) 1283.
- [51] C.C. Chong, Y.W. Cheng, S.N. Bukhari, H.D. Setiabudi, A.A. Jalil, Methane dry reforming over Ni/fibrous SBA-15 catalysts: effects of support morphology (rod-like F-SBA-15 and dendritic DFSBA-15), *Catal. Today* 375 (2021) 245–257.
- [52] R. Dębek, M. Motak, M.E. Gálvez, T. Grzybek, P. Da Costa, Promotion effect of zirconia on Mg(Ni, Al)O mixed oxides derived from hydrotalcites in CO₂ methane reforming, *Appl. Catal. B* 223 (2018) 36–46.
- [53] S.M. Sajjadi, M. Haghighi, A.A. Eslami, F. Rahmani, Hydrogen production via CO₂ reforming of methane over Cu and Co doped Ni/Al₂O₃ nanocatalyst: impregnation versus sol-gel method and effect of process conditions and promoter, *J. Sol. Gel. Sci. Technol.* 67 (2013) 601–617.
- [54] M. Shah, S. Das, A.K. Nayak, P. Mondal, A. Bordoloi, Smart designing of metal-support interface for imperishable dry reforming catalyst, *Appl. Catal. A* 556 (2018) 137–154.
- [55] R. Blom, I.M. Dahl, Å. Slagtem, B. Sortland, A. Spjelkavik, E. Tangstad, Carbon dioxide reforming of methane over lanthanum-modified catalysts in a fluidized-bed reactor, *Catal. Today* 21 (1994) 535–543.
- [56] A.M. Gaddalla, M.E. Sommer, Carbon dioxide reforming of methane on nickel catalysts, *Chem. Eng. Sci.* 44 (1989) 2825–2829.
- [57] L. Foppa, T. Margossian, S.M. Kim, C. Müller, C. Copéret, K. Larmier, A. Comas-Vives, Contrasting the role of Ni/Al₂O₃ interfaces in water-gas shift and dry reforming of methane, *J. Am. Chem. Soc.* 139 (2017) 17128–17139.
- [58] D. Chen, K.O. Christensen, E. Ochoa-Fernández, Z. Yu, B. Tødtal, N. Latorre, A. Monzón, A. Holmen, Synthesis of carbon nanofibers: effects of Ni crystal size during methane decomposition, *J. Catal.* 229 (2005) 82–96.
- [59] O. Daoura, G. Fornasier, M. Boutros, N. El Hassan, P. Beaunier, C. Thomas, M. Selmane, A. Miche, C. Sasseoye, O. Ersen, One-pot prepared mesoporous silica SBA-15-like monoliths with embedded Ni particles as selective and stable catalysts for methane dry reforming, *Appl. Catal. B* 280 (2021), 119417.
- [60] M. Li, A.C. van Veen, Tuning the catalytic performance of Ni-catalysed dry reforming of methane and carbon deposition via Ni-CeO_{2-x} interaction, *Appl. Catal. B* 237 (2018) 641–648.
- [61] M. Akri, S. Zhao, X. Li, K. Zang, A.F. Lee, M.A. Isaacs, W. Xi, Y. Gangarajula, J. Luo, Y. Ren, Atomically dispersed nickel as coke-resistant active sites for methane dry reforming, *Nat. Commun.* 10 (2019) 1–10.
- [62] J.P. Janet, S. Ramesh, C. Duan, H.J. Kulik, Accurate multiobjective design in a space of millions of transition metal complexes with neural-network-driven efficient global optimization, *ACS Cent. Sci.* 6 (2020) 513–524.
- [63] C.R. Blyth, On Simpson's paradox and the sure-thing principle, *J. Am. Stat. Assoc.* 67 (1972) 364–366.
- [64] D.H. Wolpert, Stacked generalization, *Neural Netw.* 5 (1992) 241–259.
- [65] A. Khemphila, V. Boonjing, Comparing performances of logistic regression, decision trees, and neural networks for classifying heart disease patients, 2010 Int. Conf. Comput. Inf. Syst. Ind. Manag. Appl. (CISIM), IEEE (2010) 193–198.
- [66] L. Grinsztajn, E. Oyallon, G. Varoquaux, Why do tree-based models still outperform deep learning on tabular data, *arXiv Prepr. arXiv* 2207 (2022) 08815.
- [67] Y. Gorishniy, I. Rubachev, V. Khrulkov, A. Babenko, Revisiting deep learning models for tabular data, *Adv. Neural Inf. Process. Syst.* 34 (2021) 18932–18943.
- [68] T.G. Dietterich, Ensemble methods in machine learning. International Workshop on Multiple Classifier Systems, Springer, 2000, pp. 1–15.
- [69] E.C. Carlson, Don't gamble with physical properties for simulations, *Chem. Eng. Prog.* 92 (1996) 35–46.